

Ferrielectricity controlled widely-tunable magnetoelectric coupling in van der Waals multiferroics

Received: 26 July 2023

Accepted: 27 March 2024

Published online: 08 April 2024

 Check for updates

Qifeng Hu^{1,9}, Yuqiang Huang^{1,9}, Yang Wang^{2,9}, Sujuan Ding^{3,9},
Minjie Zhang^{1,9}, Chenqiang Hua¹, Linjun Li⁴✉, Xiangfan Xu⁵, Jinbo Yang⁶,
Shengjun Yuan⁷, Kenji Watanabe⁸, Takashi Taniguchi⁸, Yunhao Lu¹✉,
Chuanhong Jin³✉, Dawei Wang² & Yi Zheng¹✉

The discovery of various primary *ferroic* phases in atomically-thin van der Waals crystals have created a new two-dimensional wonderland for exploring and manipulating exotic quantum phases. It may also bring technical breakthroughs in device applications, as evident by prototypical functionalities of giant tunneling magnetoresistance, gate-tunable ferromagnetism and non-volatile ferroelectric memory etc. However, two-dimensional multiferroics with effective magnetoelectric coupling, which ultimately decides the future of multiferroic-based information technology, has not been realized yet. Here, we show that an unconventional magnetoelectric coupling mechanism interlocked with heterogeneous ferrielectric transitions emerges at the two-dimensional limit in van der Waals multiferroic CuCrP_2S_6 with inherent antiferromagnetism and antiferroelectricity. Distinct from the homogeneous antiferroelectric bulk, thin-layer CuCrP_2S_6 under external electric field makes layer-dependent heterogeneous ferrielectric transitions, minimizing the depolarization effect introduced by the rearrangements of Cu^+ ions within the ferromagnetic van der Waals cages of CrS_6 and P_2S_6 octahedrons. The resulting ferrielectric phases are characterized by substantially reduced interlayer magnetic coupling energy of nearly 50% with a moderate electric field of 0.3 V nm^{-1} , producing widely-tunable magnetoelectric coupling which can be further engineered by asymmetrical electrode work functions.

The interplay and mutual control of multiple ferroic orders, in particularly magnetism and ferroelectricity, in a single-phase system provides a fascinating platform for both fundamental understanding on correlated phenomena and developing the next-generation non-volatile storage technologies¹. Despite the tremendous success in classifying and revealing multiferroic mechanisms in paradigmatic bulk systems, viz. type-I multiferroics with nearly independent magnetism and ferroelectricity² and type-II multiferroics originated from Dzyaloshinskii-Moriya interaction and other types of magnetic orderings such as collinear magnetic structures^{3–5}, the quest for a room-

temperature multiferroic with efficient coupling between magnetism and ferroelectricity remains as the holy grail of the resurgent field. Recent studies on magnetism and ferroelectricity in two-dimensional (2D) van der Waals (vdW) crystals open unparalleled opportunities for multiferroic research^{6–10}, considering that abundant choices of ferroic atomic layers with single-crystal quality can be readily tuned by electrostatic field, strain, interfaces and spin-lattice interactions^{11–14}. Equally important, the Lego combination of different 2D ferroic building blocks may lead to the finding of novel multiferroic phases beyond the prevailing spin-driven ferroelectric paradigm^{15,16}.

A full list of affiliations appears at the end of the paper. ✉ e-mail: lilinjun@zju.edu.cn; luyh@zju.edu.cn; chhj@zju.edu.cn; phyzhengyi@zju.edu.cn

Beyond the framework of the isotropic Heisenberg model, various vdW bulk magnets with significant magnetocrystalline anisotropy have been re-explored at the 2D limit with fruitful results, e.g., 2D CrI₃, CrCl₃, CrSBr, and CrPS₄ with interlayer antiferromagnetic (AFM) coupling and intralayer ferromagnetic (FM) ordering, layer-dependent FM in Cr₂Ge₂Te₆, CrBr₃ and Fe₃GeTe₂, and emergent intralayer AFM systems of MnPS₃ and CrOCl^{13,14,17–27}. Gate-tunable magnetic properties have also been demonstrated by electric controlled magnetic transistors of 2D Cr₂Ge₂Te₆ and memristive devices of CrI₃^{11,28}. As an electric counterpart to magnetism, 2D ferroelectricity in atomically thin vdW crystals is also not rare, such as SnTe, CuInP₂S₆, In₂Se₃, WTe₂ and bilayer boron nitrides with divergent ferroelectric mechanisms^{8,29–34}. Intriguingly, unlike bulk materials, 2D vdW systems tend to host multiple ferroic orders in one single phase, e.g., ferroelectricity and ferroelasticity predicted in monolayer group IV monochalcogenides^{35,36}, and ferromagnetism and ferroelasticity in monolayer α -SnO³⁷. Recently, the experimental implementation of a 2D magnetoelectric multiferroic was reported in NiI₂⁹, however, the electrical control of magnetism, and the vice versa, remains elusive in this system.

Belonging to the large family of metal thio- and selenophosphate vdW crystals with rich ferroic phases^{21,29,38,39}, CuCrP₂S₆ (CCPS) is a unique choice of magnetoelectric multiferroics for exploring 2D magnetism-ferroelectricity interactions with experimentally confirmed coexistence of interlayer AFM and intralayer stripe antiferroelectric (AFE) in the bulk crystals^{40–51}. As illustrated in Fig. 1a, CCPS crystals have a monoclinic lattice of the space group *Pc* (No. 7), in which a monolayer can be viewed as hexagonal vdW cages consisting of interconnected CrS₆ and P₂S₆ octahedrons. Below the Néel temperature (T_N) of ~31 K, the magnetic moments of Cr³⁺ become ferromagnetically aligned within individual monolayers, which are further

AFM coupled in perpendicular to the vdW plane (Fig. 1b). On the other hand, the ferroelectric property of CCPS is rooted in Cu⁺ ions, which are randomly distributed within the FM CrS₆-P₂S₆ cages. At 145 K, the crystal becomes AFE, when the adjacent Cu ions form striped AFE alignment driven by a double-well pseudo potential⁴¹. In the AFE state, each CCPS monolayer is characterized by a distinctive mirror symmetry along the *b*-axis, in perpendicular to the Cu⁺ AFE stripe chains.

Here, we report an unconventional magnetoelectric coupling (MEC) interlocked with electric field tunable ferroelectric (FiE) transitions in 2D multiferroic CCPS, unveiling the rich promises of discovering highly tunable 2D MEC mechanisms fundamentally different from the bulk counterparts. Using magnetic tunneling junctions (MTJs), we demonstrate the electric field control of interlayer magnetic coupling strength, when Cu⁺ ions rearrange within the CrS₆-P₂S₆ cages to form a layer-dependent heterogeneous FiE phase. The existence and continuous control of the FiE state are unambiguously proved by temperature- and polarization-dependent second harmonic generation (SHG) experiments, in which the latter unveils a fingerprinting six-fold to two-fold symmetry transition when thin-layer CCPS is driven from the AFE state into the FiE phase by an external bias voltage (V_b). The formation of the FiE phase enforces substantially lattice distortions for the CrS₆ octahedrons, which effectively modulate the interlayer superexchange coupling strength via the interlayer Cr-S-S-Cr pathways. This unique FiE-controlled MEC mechanism has a wide tunability, evident by a remarkable reduction in the interlayer magnetic coupling energy of nearly 50% with a moderate electric field of 0.3 V nm⁻¹.

Results

Due to the insulating nature, we study the layer-dependent 2D magnetism, ferroelectricity and magnetoelectric properties of CCPS based

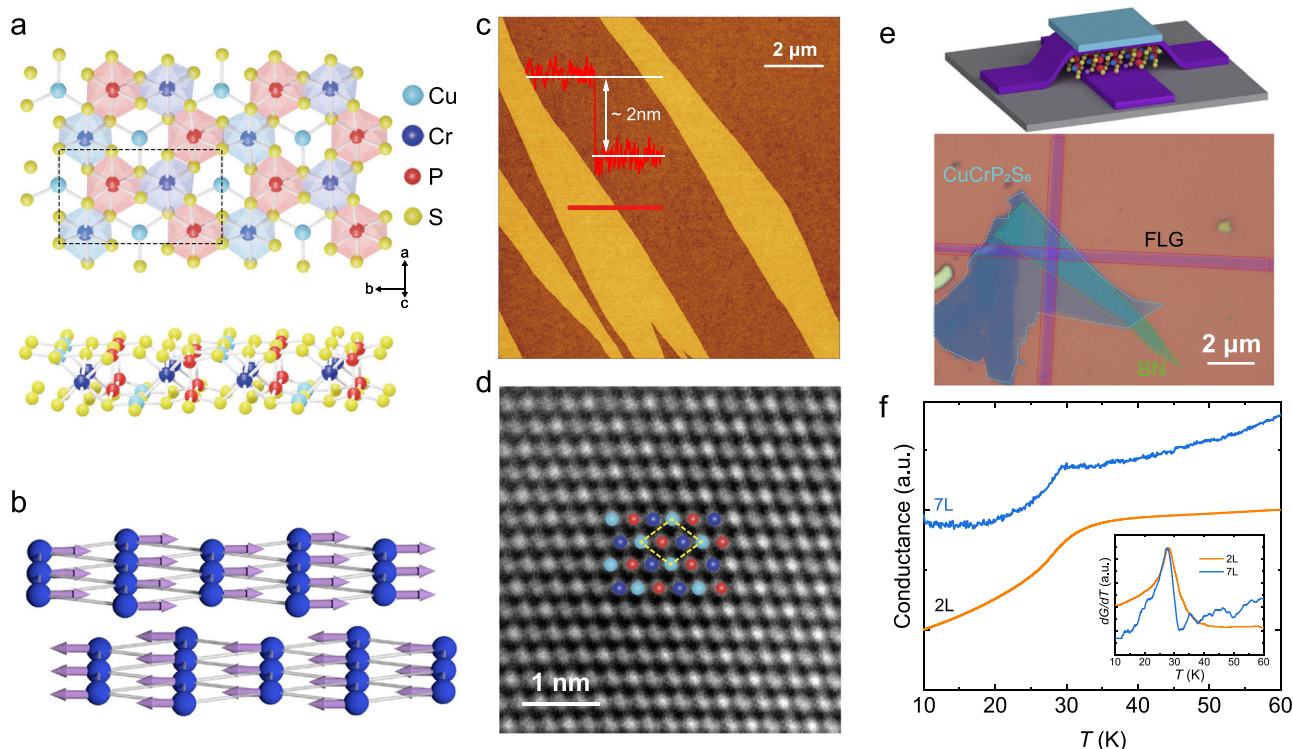


Fig. 1 | Magnetoelectric multiferroics and Cu⁺ ion polarizations in a ferro-magnetic vdW cage. **a** Top and side views of the lattice structure of a CCPS monolayer. Interconnected CrS₆ and P₂S₆ octahedrons form hexagonal vdW cages for polarizable Cu⁺ ions. **b** Schematic of the interlayer AFM order in CCPS, where only the Cr atomic layers are shown for clarity. **c** NCAFM imaging and line profiling of bilayer CCPS flakes on SiO₂/Si substrates. **d** ADF-STEM image of a BL CCPS,

showing high crystal quality without noticeable defects. **e** Top: device structure of thin-layer CCPS MTJs. Bottom: false-color optical image of a representative BL MTJ BL-S44. **f** Tunneling conductance G vs T curves of representative BL-S44 and 7L-S21. Inset: the corresponding dG/dT , revealing a thickness-independent AFM phase transition at about 30 K.

on vertical magnetic tunnel junctions, which are consisting of few-layer graphene (FLG) electrodes and thin layers of CCPS channels with consecutive thicknesses from bilayer (BL) to 10L (see Methods and Supplementary Information Note 1). Figure 1c shows the non-contact atomic force microscopy (NCAFM) of a BL CCPS sample, as evident by a 2 nm step height. Atomic-resolution annular dark-field scanning transmission electron microscopy (ADF-STEM) confirms the high crystal quality of exfoliated thin-layer CCPS samples with no apparent vacancies (Fig. 1d and Supplementary Note 1). If not specified otherwise, all tunneling results were measured at a base temperature of $T = 1.6$ K.

To investigate the magnetic phase transitions at the 2D limit, we have carried out T -dependent zero-bias tunneling experiments. As shown in Fig. 1e, f, using a small excitation current of 10 nA and zero magnetic field (H), the tunneling conductance of CCPS MTJs with different thicknesses consistently show an anomaly at ~ 30 K, in excellent agreement with the bulk T_N . The results strongly suggest that atomically thin CCPS retain the bulk AFM order, as expected for a vdW magnet with strong magnetic anisotropy. Using H -dependent tunneling spectroscopy, we observe the typical metamagnetic transition behavior for thin-layer CCPS MTJs, when interlayer Cr spin moments become symmetrically tilted along the H direction to form the canted AFM (CAFM) state^{14,24}. As shown in Fig. 2a, the tunneling current (I_t) of BL-S44 first increases smoothly as a function of in-plane H_{\parallel} , manifesting the spin-canting angle vs H evolution of the CAFM phase. In the AFM ground state, two CCPS MLs with opposite magnetization direction form a spin filter tunneling barrier equivalent for electron transmission with opposite spins, as schemed in Fig. 2b (see Supplementary Note 2 for detailed information on the spin-filter mechanism). This produces a low I_t which corresponds to a high resistance state^{52–54}. When $\mu_0 H_{\parallel}$ reaches 3.2 T, the atomic spin valve is switched to the low

resistance state due to parallel magnetization between two adjacent MLs. The resulting I_t becomes significantly enhanced attributed to asymmetric tunneling barriers for opposite spins^{24,53}. For simplicity, we will refer this magnetization saturation state as the field-aligned ferromagnetic phase (FM'), and the saturation magnetic field as H_{sat} .

Such an H -driven CAFM to FM' transition is further confirmed by T -dependent tunneling magnetoresistance (TMR), defined by $\text{TMR} = [I_t(H) - I_t(0)]/I_t(0) \times 100\%$ ^{14,24,53}. As summarized in Fig. 2c, the CAFM-FM' transitions gradually shift to lower values of H_{sat} due to increased thermal fluctuation. Above T_N , the TMR curves exhibit a negative growth rate, in consistent with a paramagnetic state. It is illuminating to plot the field derivative of TMR (dR/dH_{\parallel}) into a 2D contour image as a function of both T and H_{\parallel} , which clearly reveals the magnetic phase diagram of CCPS at the 2D limit (Fig. 2d). For CCPS MTJs with odd-layer thicknesses, for example a quintuple-layer MTJ (5L-S5), the corresponding T -dependent TMR and the 2D contour plot are shown in Fig. 2e, f, respectively. The overall phase diagram is agreeing with the BL device, indicating the same CAFM to FM' phase transitions. The distinctive odd-layer effect below 2 T is due to a field-induced perfect collinear AFM state which is first reported in few-layer CrCl_3 MTJs²⁴. Most critically, for an easy-plane magnetic anisotropy dominated vdW AFM, H_{sat} is directly proportional to the interlayer exchange coupling energy J_{\perp} ²⁴. Compared to CrCl_3 with the same thickness, H_{sat} of CCPS is nearly three times higher, which is crucial for the observation of the FiE-interlocked MEC mechanism.

Remarkably, CCPS MTJs show V_b polarity-dependent H_{sat} , which reaches a prominent change of 50% with a moderate electric field (E) of 0.3 V nm^{-1} for octuple-layer CCPS. As shown in Fig. 3a for MTJ 8L-S20, the normalized TMR curves exhibit an H_{sat} value of 5.9 T for $V_b = -1.2 \text{ V}$, which drastically changes to 8.8 T for $V_b = 1.2 \text{ V}$ (see Supplementary Note 3 for TMR normalization procedures). Distinct from a

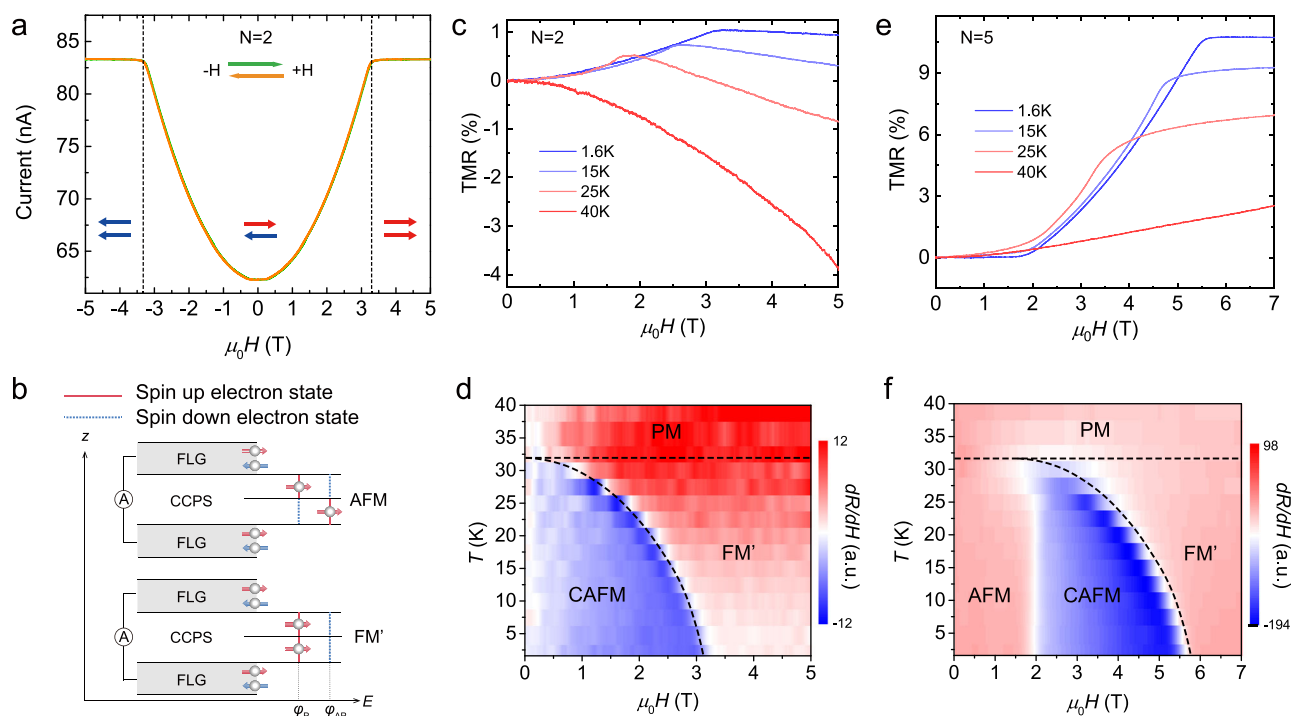


Fig. 2 | Layer-dependent metamagnetism and even-odd effects in thin-layer CCPS. **a** Tunneling current I_t vs in-plane magnetic field H_{\parallel} characteristics of a representative bilayer MTJ (BL-S44). BL-S44 exhibits a CAFM saturation field of 3.3 T, which is typical for BL devices. Here, green and orange arrows indicate the H_{\parallel} ramping directions. **b** Illustration of the multiple spin-filter effect in vdW magnets with interlayer AFM ordering. **c** T -dependent TMR vs H_{\parallel} of BL-S44, showing the dwindling of the CAFM saturation field when approaching T_N . **d** 2D contour plotting

of the first derivative of TMR (dR/dH) vs H_{\parallel} and T for BL-S44. By taking the derivative, the magnetic phase diagram of BL CCPS is clearly revealed. **e** T -dependent TMR vs H_{\parallel} of quintuple-layer MTJ (5L-S12), showing the same dwindling of H_{sat} when approaching T_N . **f** 2D contour of dR/dH vs H_{\parallel} and T for 5L-S12. Below 2 T, the magnetic phase diagram of odd-layer CCPS is characterized by a low-field perfect collinear AFM zone, i.e., the odd-layer effect.

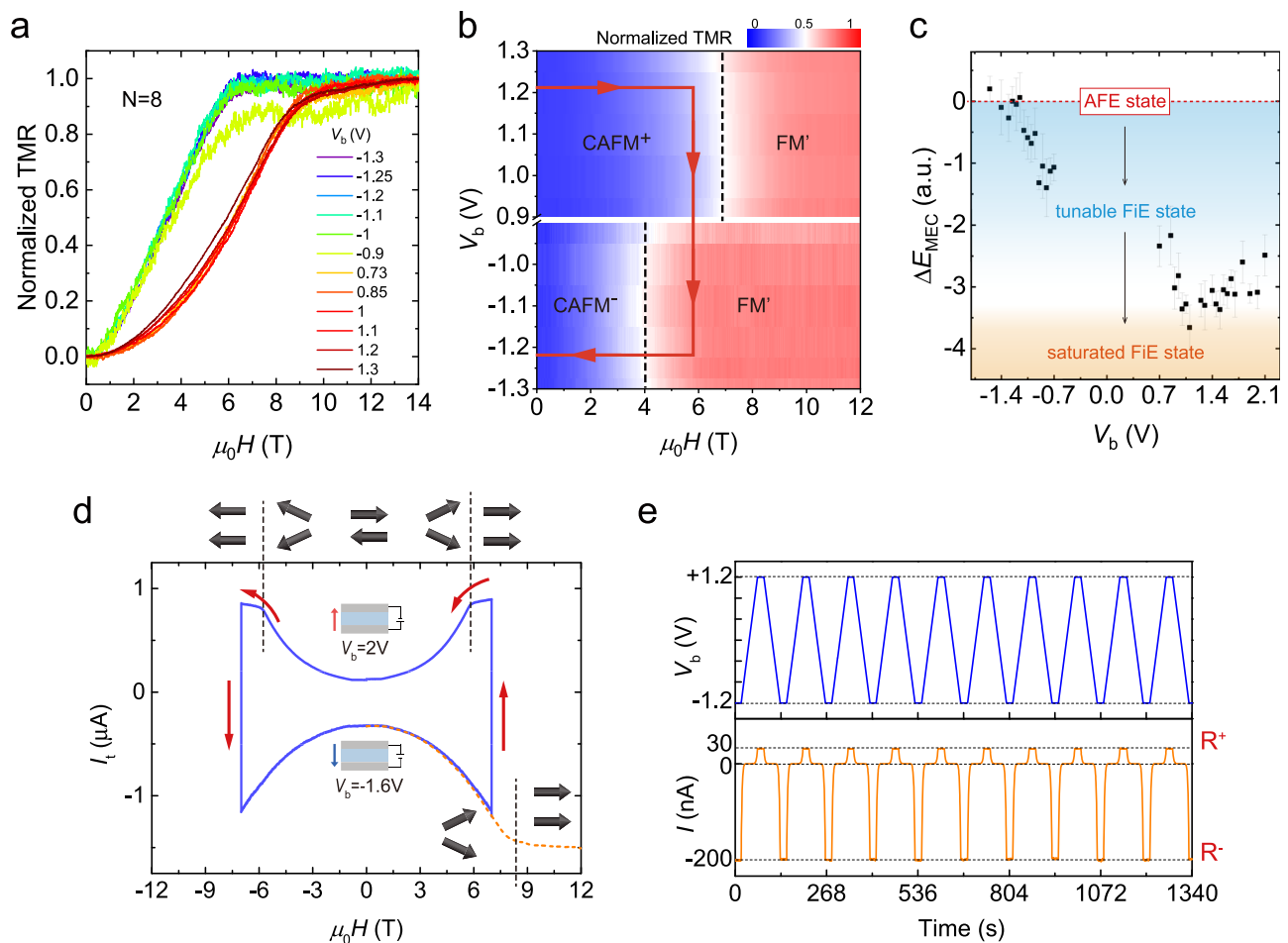


Fig. 3 | Ultra-wide V_b -tunability of magnetoelectric coupling in thin-layer CCPS. **a** Normalized TMR vs H_{\parallel} curves of MTJ 8L-S20 under different V_b setpoints. **b** 2D contour plot of the normalized TMR vs V_b and H_{\parallel} in (a). It is noteworthy that for each H_{\parallel} setpoint, the CAFM canting angle θ^{\pm} for opposite-polarity V_b are divergent (see Supplementary Fig. 5 for CAFM θ^{\pm} calculations). **c** $\Delta E_{\text{MEC}}(\mathbf{E})$ vs V_b , extracted from the TMR data of 10L-S39, and the error bars are defined as the $\pm 10\%$ variation

of half-maximum points in dG/dH curve (see Supplementary Figs. 5 and 6). **d** Dichotomic I_t vs H_{\parallel} characteristics of 8L-S20. Note that I_t is symmetric on H_{\parallel} ramping, excluding any ferroelectric polarization reversal. **e** Zero- HR_0^{\pm} reversals by switching the V_b polarities. It is apparent that the $I_t - V_b$ sweeping is completely free of hysteresis.

paraelectric dielectric response, the V_b -dependence is conspicuously non-linear, which can be divided into two opposite-polarity regimes of 0.73 to 1.3 V for high $H_{\text{sat}}^+ = 8.8$ T and -0.9 to -1.3 V for low $H_{\text{sat}}^- = 5.9$ T, respectively. The dichotomic polarity behavior in V_b and the wide tunability of H_{sat} are best visualized by a 2D contour plot of TMR vs both V_b and H . As shown in Fig. 3b, the large H_{sat} window between positive and negative V_b polarities opens a new possibility to directly manipulate the magnetic state of CCPS MTJs by V_b , i.e., the electrical control of magnetism. Indeed, by sweeping V_b and H to follow the path indicated by red solid lines in Fig. 3b, we can readily enforce a FM' to CAFM phase transition, and the vice versa, simply by reversing the V_b polarities. Since H_{sat} represents the interlayer coupling energy J_{\perp} , we can directly measure the change of MEC energy introduced by V_b -polarity reversal by $\Delta E_{\text{MEC}} \propto (H_{\text{sat}}^+ - H_{\text{sat}}^-)$. Detailed TMR study reveals that in between H_{sat}^{\pm} , H_{sat} is continuously tuned by V_b setpoints before reaching the binary saturation values (Fig. 3c and detailed discussions in Supplementary Note 4). The large ΔE_{MEC} of ~ 1.08 meV per unit-cell (UC) explains the bistable magnetoresistance states TMR^{\pm} for $H \neq 0$ (Fig. 3d). However, within the same AFM ground state, zero- H resistance states R_0^{\pm} remain binary valued, which can be reproducibly switched by reversing the V_b polarities, as shown in Fig. 3e for MTJ 10L-S39.

Such an unexpected reversal behavior in R_0^{\pm} reminds us the importance of the inherent stripe-AFE phase of CCPS, in analogy with

the resistance switching of graphene-ferroelectric field-effect transistors (GFeFETs) under a constant electrostatic doping^{55,56}. However, unlike the hysteretic two-state switching in GFeFETs controlled by ferroelectric polarization reversals^{55,56}, the stripe-AFE phase of CCPS requires an enormous energy to be fully polarized, which can be evaluated quantitatively by the first-principle density-functional theory (DFT) calculations. As shown in Fig. 4a, an FE configuration for a BL UC will unrealistically increase the system energy by 337 meV per UC when compared with the stripe-AFE ground state (see Method for the calculation details). From the thermodynamic point of view, the FE state is also not favored due to the maximization of the depolarization effect, as depicted by the black hollow arrows. Based on DFT calculations, it is also not feasible to locally flip an AFE stripe by \mathbf{E} within a single vdW ML. For BL CCPS, the lowest metastable state is to flip the anti-parallel stripes of the bottom ML toward the vdW interface, corresponding to a largely reduced energy requirement of 95 meV per UC (2L-mAFE-I). In Fig. 4b, we plot the energy potential diagram of BL CCPS as a function of the displacement (Δd) of the anti-parallel Cu-ion stripes within the bottom ML, suggesting a rapid growth in the system energy by approaching the Cr atomic plane. Note that even with the presence of an impractical \mathbf{E} of 2 V nm^{-1} , the energy of 2L-mAFE-I remains substantially higher than the AFE ground state, and the energy barrier in-between is far too high to be crossed by Cu^+ ions (Supplementary Note 5).

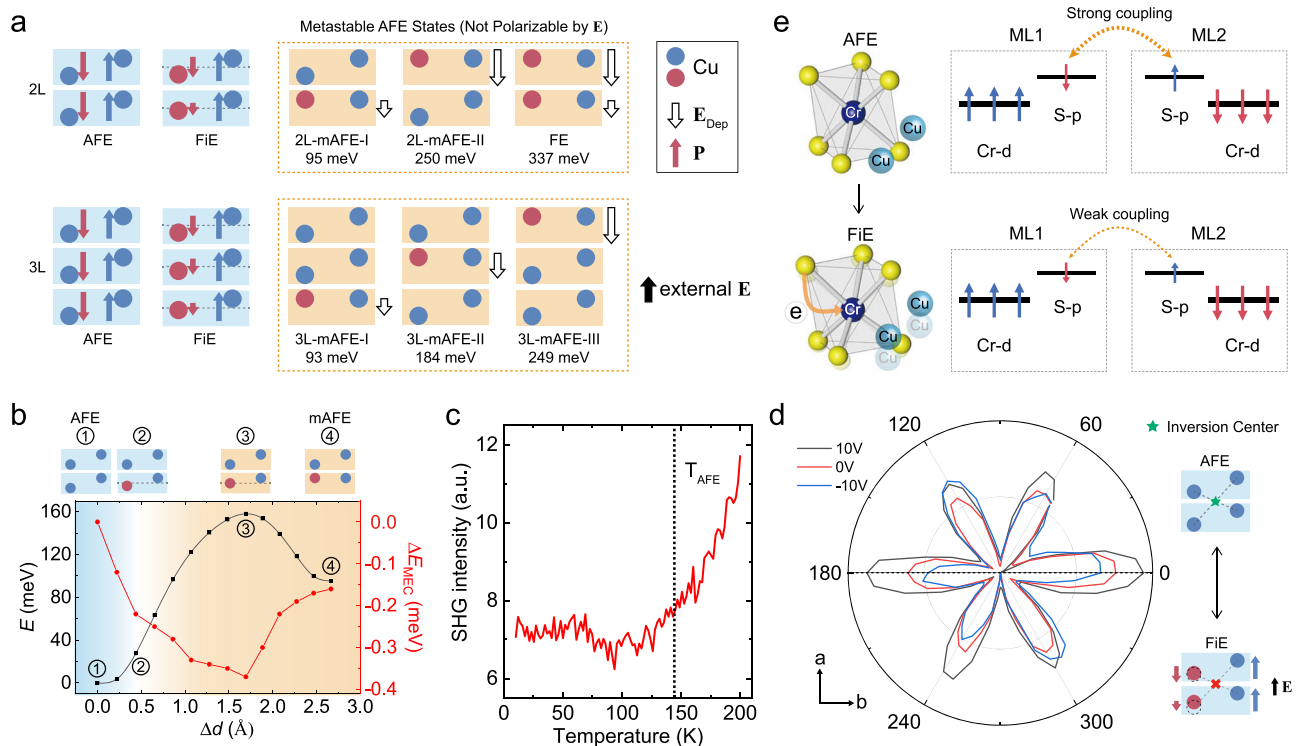


Fig. 4 | Ferrielectricity controlled magnetoelectric coupling in thin-layer CCPS.

a Lattice model representation of the stripe-AFE state (first column), the E-enforced heterogeneous FIE phase (second column), and energy unfavorable metastable AFE states (third column; grouped in orange dashed lines) for BL and trilayer CCPS, respectively. Here, the vdW monolayer cages are represented by blue/orange rectangles, standing for energy accessible and inaccessible respectively. Within the cages, the ground-state (polarized) Cu^+ ions are depicted by blue (red) circles. Here, 2L-mAFE-I and 2L-mAFE-II correspond to the flipping of an anti-parallel Cu-ion stripe of within the bottom and top ML, respectively. **b** Black curve: Energy potential diagram vs Δd (anti-parallel Cu^+ displacement) of BL CCPS from the AFE

ground state to 2L-mAFE-I. Red curve: ΔE_{MEC} on Δd , which monotonically decreases when Cu^+ ions move towards the Cr atomic plane. **c** SHG intensity vs T , showing the AFE transition and the frozen of Cu^+ ions at around 140 K. **d** Polarization-dependent SHG at 77 K under different V_b . The distinctive six-fold to two-fold transition in the polarization-SHG patterns proves that the non-linear optical anisotropy of thin-layer CCPS associated with inversion symmetry breaking can be continuously tuned by V_b . **e** Illustration of the FIE-interlocked MEC mechanism in CCPS, in which lattice distortions introduced by Cu^+ ion displacements efficiently lower the interlayer superexchange interaction.

Indeed, for all CCPS MTJs, the $I_t - V_b$ characteristics measured with various H setpoints (Supplementary Note 6) are thoroughly free of hysteresis behaviors, in consistent with the DFT calculations that predict no metastable phase transition under realistic \mathbf{E} values. The DFT-based analyses of flipping a minimal AFE stripe can be readily extended to different ML numbers, as shown in the bottom panels of Fig. 4a for trilayer CCPS (quadruple-layer in Supplementary Note 5). With increased layer numbers, different metastable states can be used as an ML index of the flipped AFE stripe, whose energy cost is closely related to a peculiar layer-dependent depolarization mechanism. Using BL CCPS as an example, by flipping one AFE stripe in the top ML, the energy requirement of 2L-mAFE-II is drastically increased by nearly four times to 250 meV per UC, when compared with 2L-mAFE-I. The large energy difference between 2L-mAFE-I and 2L-mAFE-II is due to the fact that, for the former, the local flipped AFE domain is effectively screened by the neighboring AFE ML to minimize the depolarization field. Such a unique dipole screening mechanism for vdW ferroelectrics, designated as the vdW depolarization effect hereafter, can be well reproduced by DFT calculations of layer-dependent charge density distribution in response to AFE stripe displacements (see Supplementary Note 5 for details).

Although the metastable AFE states are not energy accessible by experimental \mathbf{E} , the CCPS lattice spontaneously responds to the external electric field by readjusting the positions of Cu^+ ions within the vdW cages of CrS_6 and P_2S_6 octahedrons. Our DFT calculations reveal that, the polarizations are predominated by layer-dependent rearrangements of the anti-parallel Cu^+ ions, leading the formation

of a heterogeneous FIE state. As schemed in the second column of Fig. 4a, due to the unique vdW depolarization effect, anti-parallel Cu^+ ions in different MLs will move toward the Cr atomic plane under \mathbf{E} , with Δd proportional to the energy of the ML-indexed metastable AFE states. The formation of an E-dependent FIE state is confirmed by SHG experiments, with tunable V_b applied to the heterostructures of FLG/BN/CCPS/BN/FLG. As shown in Fig. 4c, by cooling down a 6L device, the T -dependent SHG intensity decreases monotonically and eventually stabilizes at about 140 K, which manifests the AFE transition of thin-layer CCPS when Cu^+ ions lock into the stripe-AFE positions. We also conduct polarization-dependent SHG measurements at 300 K and 77 K, respectively, with different V_b setpoints. Strikingly, polarization-SHG at 77 K unveils a fingerprinting six-fold to two-fold symmetry transition when thin-layer CCPS under \mathbf{E} is driven from the AFE state into the FIE phase (Fig. 4d). In stark contrast, the same CCPS device at 300 K consistently shows a nearly six-fold symmetry for different V_b (Supplementary Fig. 14c). Similar results are well reproduced on multiple devices, and also repeated on an FLG/CCPS/ SiO_2 /Si structure, in which the heavily doped silicon substrate was used as the bias electrode. The V_b -dependent SHG intensity reflects continuous inversion symmetry breaking induced by \mathbf{E} . As illustrated in the insets of Fig. 4d, for the stripe-AFE ground state, there exists an inversion center between two neighboring monolayers, while the V_b -driven heterogeneous FIE state has reduced inversion symmetry due to layer-dependent rearrangements of anti-parallel Cu^+ ions within the FM vdW cages.

Most unusually, the formation of **E**-dependent heterogenous FiE state is accompanied by a significant reduction in the magnetic energy difference between the interlayer FM' and AFM configurations, which manifests the change of V_b -tunable MEC energy ΔE_{MEC} . Using the illustrative example of BL CCPS, the DFT calculations deduce that the FiE state has monotonically decreased $\Delta E_{\text{MEC}}(\mathbf{E})$, defined by $\Delta E_{\text{MEC}}(\mathbf{E}) = (E_{\text{FM}}(\mathbf{E}) - E_{\text{AFM}}(\mathbf{E})) - (E_{\text{FM}}(0) - E_{\text{AFM}}(0))$, when **E** drives anti-parallel positioned Cu^+ ions toward the energy saddle point of the Cr atomic plane (see Supplementary Note 7 for the detailed formulation of $\Delta E_{\text{MEC}}(\mathbf{E})$). As illustrated in Fig. 4e, for thin-layer CCPS, the interlayer superexchange that determines J_{\perp} is intermediated by the interfacial majority spin *p*-orbitals of S atoms, which are antiparallel to the Cr magnetic moments due to the formation of Cr-S valence bonds⁵⁷. The stripe-AFE ground state corresponds to a relative symmetric CrS_6 octahedron with minimal lattice distortions (Fig. 4e and DFT calculations in Supplementary Table 1). In response to external electric field, anti-parallel Cu^+ ions move within the FM vdW cages, enforcing substantially lattice distortions for the CrS_6 octahedrons by stretching the average Cr-S bond lengths. The resulting attenuation of the Cr-S bonding energy effectively decreases the net majority spins of S atoms, which changes from 0.135 electrons per S for $d = 0 \text{ \AA}$ (the equilibrium stripe-AFE position) to 0.092 electrons per S for $\Delta d = 0.44 \text{ \AA}$, and thus, efficiently lowers the interlayer AFM coupling.

As summarized in Fig. 4b, the collective movements of anti-parallel Cu^+ ions within the FM vdW cages reach the maximum ΔE_{MEC} of -0.37 meV for the saddle point position $\Delta d = 1.69 \text{ \AA}$. It should be noted that $\Delta E_{\text{MEC}}(\mathbf{E})$ has a maximized change rate within the **E**-polarizable regime, which is highlighted by the blue color ($\mathbf{E} < 1.5 \text{ V nm}^{-1}$; see Supplementary Note 6 for electric breakdown test). In this polarization regime, ΔE_{MEC} rapidly reaches -0.15 meV for a minute Δd of 0.29 \AA , which is qualitatively in agreement with the experimental ΔE_{MEC} estimated by H_{sat}^{\pm} . As a direct consequence of this ultra V_b -tunable ΔE_{MEC} , the V_b -dependent heterogenous FiE state has drastically reduced J_{\perp} , which changes by nearly 50% with a moderate **E** of 0.3 V nm^{-1} as shown in Fig. 3c. After elucidating the V_b -tunable MEC mechanism, the final key element is to understand the V_b -polarity asymmetry in the MEC coupling, which is attributed to a build-in potential introduced by the asymmetric work functions of top and bottom FLG electrodes. Using Fowler-Nordheim (FN) tunneling in complementary with scanning Kelvin probe microscope (SKPM), we determined that the asymmetric work functions can readily reach 0.5 eV due to the Dirac electronic structure of graphene and the interfacial doping by AFE CCPS flakes^{55,56} (see Supplementary Note 4 and Note 8 for detailed analyses using FN tunneling and SKPM). As shown in Supplementary Fig. 7a, the existence of a build-in potential makes the two otherwise V_b -polarity equivalent FiE states asymmetric in energy, in analogy to GFETs under a constant electrostatic doping^{55,56}.

Discussion

The striking energy difference between the 2L-mAFE-I and 2L-mAFE-II states of BL CCPS provide an amazing example on how the well-established depolarization mechanism may become peculiarly different at the 2D limit in a vdW multiferroic. The discovered FiE interlocked widely-tunable MEC mechanism also suggests the great potential of realizing highly-efficient electric control of 2D magnetism in emergent vdW multiferroics. Equally important, the multiferroicity in thin-layer CCPS opens the possibility for the investigation of 2D quantum phase transitions, and the fabrication of complex vdW heterostructure for the realization of two-phase multiferroic for novel electronically controlled spintronics and Josephson junctions.

Methods

Crystal growth

Bulk CCPS single crystals were synthesized by the standard self-flux method. High purity Cu (99.999%), Cr (99.996%), P (99.999%) and S

(99.5%) powders were mixed stoichiometrically and loaded into a quartz tube in an argon-filled glove box. The quartz tube was evacuated to a pressure of 10^{-2} Pa before flame-sealing and placing into a tube furnace. For crystal growth, the temperature was ramped from room-temperature to 973 K , which was held constant for 14 days by PID control. After that, the furnace was naturally cooled to room temperature.

Tunneling junction fabrications

CCPS MTJs were fabricated in an argon-filled glove box. Different thicknesses of CCPS flakes were exfoliated from single-crystal seeds, identified by optical contrast and further cross checked by atomic force microscopy (Park system NX10) and Raman spectroscopy. To obtain a MTJ shown in Fig. 1e, thin-layer CCPS flakes were exfoliated on SiO_2/Si substrates, followed by two PC/PDMS based dry-transfer steps³⁸ to prepare the top and bottom few-layer graphene (FLG) electrodes. In the final step, the MTJ is covered by a thin-film flake of hexagonal boron nitride to protect the sample from ambient exposure. Top and bottom FLG electrodes were contacted by $5/50 \text{ nm}$ Cr/Au electrode using standard electron beam lithography (EBL) technique followed by thermal evaporation.

Electrical measurements

Electrical measurements were performed in an Oxford-14 T cryostat. The system is equipped with a sample rotator for applying magnetic field either in-plane or out-of-plane. The *I*-*V* curve were measured using a Keithley 2400 and zero-bias-resistance were measure by using standard lock-in method (with excitation frequency $< 20 \text{ Hz}$).

SHG measurements

The SHG measurements are conducted in a liquid nitrogen cooled optical cryostat with a femtosecond laser (Rainbow OEM, NPI Lasers). The wavelength is centered at either 1064 nm or 1560 nm , both yielding consistent SHG results. The laser beam is focused on the samples with a near-infrared radiation (NIR) objective (MplanApo NIR 50x, OptoSigma) and collected in a reflective geometry, wherein the SHG signal is separated with a dichroic mirror. The signal is detected with a fiber coupled spectrometer (UHTS 600 VIS, Witec). For polarization-dependent SHG measurements, the polarization angle between the incident laser and the SHG signal is set by two polarizers, and the in-plane polarization direction is rotated by a dual band half-wave plate before the optical objective. The optic setup is schematically illustrated in Supplementary Fig. 14d. The signals are confirmed to be originating in the CCPS samples by comparing with the reference spectra from BN, FLG electrodes and SiO_2 areas on the substrates.

DFT calculations

The first-principles DFT calculations were performed using the Vienna ab initio simulation package (VASP) with the choice of projector augmented waves (PAW) basis set⁵⁹⁻⁶¹. The Perdew-Burke-Ernzerh (PBE) functional has been employed to treat the exchange and correlation functional⁶². The energy cut off for the plane-wave basis was set to 600 eV . All the structures were fully relaxed until the force on every atom and energy were converged to 0.01 e \AA^{-1} and $1 \times 10^{-7} \text{ eV}$, respectively. A Γ -centred Monkhorst-Pack $12 \times 8 \times 1$ k-mesh was used for k-point sampling⁶³. To model the 2D films, a vacuum layer of at least 20 \AA was included in the *c*-axis direction. The Hubbard correction of $U = 3 \text{ eV}$ is applied to the $3d$ orbitals of Cr⁶⁴. The vdW corrections were included by the DFT-D3 method⁶⁵. The kinetic pathways were calculated by the climbing image nudged elastic band (CINEB) method⁶⁶.

Layer-dependent CAFM saturation field H_{sat}

For in-plane H_{\parallel} , the magnetization of each ML (M_s) lies within the vdW plane, which can be described by a 1D spin-chain model²⁴. By labeling the magnetization of the *i*th layer as $\mathbf{M}_i = M_s(\cos \theta_i, \sin \theta_i, 0)$, where θ_i is

32. Fei, Z. et al. Ferroelectric switching of a two-dimensional metal. *Nature* **560**, 336–339 (2018).
33. Yasuda, K., Wang, X., Watanabe, K., Taniguchi, T. & Jarillo-Herrero, P. Stacking-engineered ferroelectricity in bilayer boron nitride. *Science* **372**, 1458–1462 (2021).
34. Stern, M. V. et al. Interfacial ferroelectricity by van der Waals sliding. *Science* **372**, 1462–1466 (2021).
35. Fei, R., Kang, W. & Yang, L. Ferroelectricity and phase transitions in monolayer group-IV monochalcogenides. *Phys. Rev. Lett.* **117**, 097601 (2016).
36. Wang, H. & Qian, X. Two-dimensional multiferroics in monolayer group IV monochalcogenides. *2D Mater.* **4**, 015042 (2017).
37. Seixas, L., Rodin, A. S., Carvalho, A. & Castro Neto, A. H. Multiferroic two-dimensional materials. *Phys. Rev. Lett.* **116**, 206803 (2016).
38. Susner, M. A., Chyashnavichyus, M., McGuire, M. A., Ganesh, P. & Maksymovych, P. Metal thio- and selenophosphates as multifunctional van der Waals layered materials. *Adv. Mater.* **29**, 1602852 (2017).
39. Lee, J.-U. et al. Ising-type magnetic ordering in atomically thin FePS₃. *Nano Lett.* **16**, 7433–7438 (2016).
40. Colombet, P., Leblanc, A., Danot, M. & Rouxel, J. Structural aspects and magnetic properties of the lamellar compound Cu_{0.50}Cr_{0.50}PS₃. *J. Solid State Chem.* **41**, 174–184 (1982).
41. Maisonneuve, V., Payen, C. & Cajipe, V. B. On CuCrP₂S₆: copper disorder, stacking distortions, and magnetic ordering. *J. Solid State Chem.* **116**, 208–210 (1995).
42. Kleemann, W., Shvartsman, V. V., Borisov, P., Banys, J. & Vysochanskii, Y. M. Magnetic and polar phases and dynamical clustering in multiferroic layered solid solutions CuCr_{1-x}In_xP₂S₆. *Phys. Rev. B* **84**, 094411 (2011).
43. Dziaugys, A. et al. Phase diagram of mixed Cu(In_xCr_{1-x})P₂S₆ crystals. *Phys. Rev. B* **85**, 134105 (2012).
44. Lai, Y. et al. Two-dimensional ferromagnetism and driven ferroelectricity in van der Waals CuCrP₂S₆. *Nanoscale* **11**, 5163–5170 (2019).
45. Selter, S. et al. Crystal growth, exfoliation, and magnetic properties of quaternary quasi-two-dimensional CuCrP₂S₆. *Phys. Rev. Mater.* **7**, 033402 (2023).
46. Wang, X. et al. Electrical and magnetic anisotropies in van der Waals multiferroic CuCrP₂S₆. *Nat. Commun.* **14**, 840 (2023).
47. Ma, R.-R. et al. Nanoscale mapping of Cu-ion transport in van der Waals layered CuCrP₂S₆. *Adv. Mater. Int.* **9**, 2101769 (2022).
48. Park, C. B. et al. Observation of spin-induced ferroelectricity in a layered van der Waals antiferromagnet CuCrP₂S₆. *Adv. Electron. Mater.* **8**, 2101072 (2022).
49. Cho, K. et al. Tunable ferroelectricity in van der Waals layered antiferroelectric CuCrP₂S₆. *Adv. Funct. Mater.* **32**, 2204214 (2022).
50. Hua, C. et al. Strong coupled magnetic and electric ordering in monolayer of metal thio(seleno)phosphates. *Chin. Phys. Lett.* **38**, 077501 (2021).
51. Io, W. F. et al. Direct observation of intrinsic room-temperature ferroelectricity in 2D layered CuCrP₂S₆. *Nat. Commun.* **14**, 7304 (2023).
52. Worledge, D. C. & Geballe, T. H. Magnetoresistive double spin filter tunnel junction. *J. Appl. Phys.* **88**, 5277–5279 (2000).
53. Klein, D. R. et al. Probing magnetism in 2D van der Waals crystalline insulators via electron tunneling. *Science* **360**, 1218–1222 (2018).
54. Song, T. et al. Giant tunneling magnetoresistance in spin-filter van der Waals heterostructures. *Science* **360**, 1214–1218 (2018).
55. Zheng, Y. et al. Gate-controlled nonvolatile graphene-ferroelectric memory. *Appl. Phys. Lett.* **94**, 163505 (2009).
56. Zheng, Y. et al. Graphene field-effect transistors with ferroelectric gating. *Phys. Rev. Lett.* **105**, 166602 (2010).
57. Wang, C. et al. Bethe-slater-curve-like behavior and interlayer spin-exchange coupling mechanisms in two-dimensional magnetic bilayers. *Phys. Rev. B* **102**, 020402 (2020).
58. Zomer, P. J., Guimarães, M., Brant, J. C., Tombros, N. & Van Wees, B. J. Fast pick up technique for high quality heterostructures of bilayer graphene and hexagonal boron nitride. *Appl. Phys. Lett.* **105**, 013101 (2014).
59. Kresse, G. & Furthmüller, J. Efficient iterative schemes for ab initio total-energy calculations using a plane-wave basis set. *Phys. Rev. B* **54**, 11169 (1996).
60. Kresse, G. & Furthmüller, J. Efficiency of ab-initio total energy calculations for metals and semiconductors using a plane-wave basis set. *Comput. Mater. Sci.* **6**, 15–50 (1996).
61. Blöchl, P. E. Projector augmented-wave method. *Phys. Rev. B* **50**, 17953 (1994).
62. Perdew, J. P., Burke, K. & Ernzerhof, M. Generalized gradient approximation made simple. *Phys. Rev. Lett.* **77**, 3865 (1996).
63. Monkhorst, H. J. & Pack, J. D. Special points for Brillouin-zone integrations. *Phys. Rev. B* **13**, 5188 (1976).
64. Dudarev, S. L., Botton, G. A., Savrasov, S. Y., Humphreys, C. J. & Sutton, A. P. Electron-energy-loss spectra and the structural stability of nickel oxide: an LSDA+U study. *Phys. Rev. B* **57**, 1505 (1998).
65. Grimme, S., Ehrlich, S. & Goerigk, L. Effect of the damping function in dispersion corrected density functional theory. *J. Comput. Chem.* **32**, 1456 (2011).
66. Henkelman, G., Uberuaga, B. P. & Jónsson, H. A climbing image nudged elastic band method for finding saddle points and minimum energy paths. *J. Chem. Phys.* **113**, 9901–9904 (2000).

Acknowledgements

This work is supported by the National Key R&D Program of the MOST of China (Grant Nos. 2023YFA1406302, and 2019YFA0308602), the National Science Foundation of China (Grant Nos. 12374194, 11574264, 12241401 and 12174336), and the Zhejiang Provincial Natural Science Foundation (D19A040001). Y.Z. acknowledges support from the Users with Excellence Project of Hefei Science Center CAS, 2021HSC-UE007. This work made use of the resources of the Center of Electron Microscopy of Zhejiang University.

Author contributions

Y.Z. initiated and supervised the project. Q.F.H. and M.J.Z. synthesized and characterized CCPS crystals. Q.F.H., M.J.Z. and Y.W. fabricated CCPS devices and carried out all the measurements. S.J.D. and C.H.J. did the ADF-STEM experiments. Y.Q.H., C.Q.H. and Y.H.L. did the DFT calculations. T.T. and K.W. synthesized the hBN crystals. X.F.X., J.B.Y., S.J.Y. and D.W.W. discussed the results and commented on the manuscript. Q.F.H., Y.Q.H., Y.W., L.J.L. and Y.Z. analysed the data and wrote the paper with inputs from all authors.

Competing interests

The authors declare no competing interests.

Additional information

Supplementary information The online version contains supplementary material available at <https://doi.org/10.1038/s41467-024-47373-7>.

Correspondence and requests for materials should be addressed to Linjun Li, Yunhao Lu, Chuanhong Jin or Yi Zheng.

Peer review information *Nature Communications* thanks Bingcheng Luo, Soonyong Park and Hailin Peng for their contribution to the peer review of this work. A peer review file is available.

Reprints and permissions information is available at <http://www.nature.com/reprints>

Publisher's note Springer Nature remains neutral with regard to jurisdictional claims in published maps and institutional affiliations.

Open Access This article is licensed under a Creative Commons Attribution 4.0 International License, which permits use, sharing, adaptation, distribution and reproduction in any medium or format, as long as you give appropriate credit to the original author(s) and the source, provide a link to the Creative Commons licence, and indicate if changes were made. The images or other third party material in this article are included in the article's Creative Commons licence, unless indicated otherwise in a credit line to the material. If material is not included in the article's Creative Commons licence and your intended use is not permitted by statutory regulation or exceeds the permitted use, you will need to obtain permission directly from the copyright holder. To view a copy of this licence, visit <http://creativecommons.org/licenses/by/4.0/>.

© The Author(s) 2024

¹School of Physics, and State Key Laboratory of Silicon and Advanced Semiconductor Materials, Zhejiang University, Hangzhou 310027, China. ²Zhejiang Province Key Laboratory of Quantum Technology and Device, School of Physics, Zhejiang University, Hangzhou 310027, China. ³State Key Laboratory of Silicon and Advanced Semiconductor Materials, Zhejiang University, Hangzhou 310027, China. ⁴State Key Laboratory of Extreme Photonics and Instrumentation, College of Optical Science and Engineering, Zhejiang University, Hangzhou 310027, China. ⁵School of Physics Science and Engineering, Tongji University, Shanghai 200092, China. ⁶State Key Laboratory for Mesoscopic Physics, School of Physics, Peking University, Beijing 100871, China. ⁷School of Physics and Technology, Wuhan University, Wuhan 430072, China. ⁸National Institute for Materials Science, 1-1 Namiki, Tsukuba 305-0044, Japan. ⁹These authors contributed equally: Qifeng Hu, Yuqiang Huang, Yang Wang, Sujuan Ding, Minjie Zhang. ✉ e-mail: lilinjun@zju.edu.cn; luyh@zju.edu.cn; chhjin@zju.edu.cn; phyzhengyi@zju.edu.cn